OzDES Reverberation Mapping Programme: Mg II lags and $R-L$ relation

Zhefu Yu [,1]★ Paul Martini,[1,2,3] A. Penton [,4] T. M. Davis [,4,5] C. S. Kochanek,[1,2] G. F. Lewis [,6] C. Lidman [,5,7] U. Malik [,8] R. Sharp,[8] B. E. Tucker,[5,8] M. Aguena [,9] J. Annis,[10] E. Bertin [,11,12] S. Bocquet,[13] D. Brooks,[14] A. Carnero Rosell [,9,15,16] D. Carollo,[5,17] M. Carrasco Kind [,18,19] J. Carretero [,20] M. Costanzi [,17,21,22] L. N. da Costa,[9] M. E. S. Pereira,[23] J. De Vicente [,24] H. T. Diehl,[10] P. Doel,[14] S. Everett,[25] I. Ferrero [,26] J. García-Bellido [,27] M. Gatti,[28] D. W. Gerdes,[29,30] D. Gruen [,13] R. A. Gruendl,[18,19] J. Gschwend,[9,31] G. Gutierrez,[10] S. R. Hinton [,4] D. L. Hollowood [,32] K. Honscheid,[2,33] D. J. James,[34] K. Kuehn,[7,35] J. Mena-Fernández,[24] F. Menanteau,[18,19] R. Miquel,[20,36] B. Nichol,[37] F. Paz-Chinchón,[19,38] A. Pieres [,9,31] A. A. Plazas Malagón [,39] M. Raveri,[28] A. K. Romer,[40] E. Sanchez,[24] V. Scarpine,[10] I. Sevilla-Noarbe,[24] M. Smith [,41] E. Suchyta [,42] M. E. C. Swanson,[14,34] G. Tarle,[30] M. Vincenzi,[41,43] A. R. Walker[44] and N. Weaverdyck [30,45]

Affiliations are listed at the end of the paper

ABSTRACT

The correlation between the broad line region radius and continuum luminosity (R–L relation) of active galactic nuclei (AGNs) is critical for single-epoch mass estimates of supermassive black holes (SMBHs). At $z \sim 1$–2, where AGN activity peaks, the R–L relation is constrained by the reverberation mapping (RM) lags of the Mg II line. We present 25 Mg II lags from the Australian Dark Energy Survey RM project based on 6 yr of monitoring. We define quantitative criteria to select good lag measurements and verify their reliability with simulations based on both the damped random walk stochastic model and the rescaled, resampled versions of the observed light curves of local, well-measured AGN. Our sample significantly increases the number of Mg II lags and extends the R–L relation to higher redshifts and luminosities. The relative iron line strength $\mathcal{R}_{\mathrm{Fe}}$ has little impact on the R–L relation. The best-fitting Mg II R–L relation has a slope $\alpha = 0.39 \pm 0.08$ with an intrinsic scatter $\sigma_{\mathrm{rl}} = 0.15^{+0.03}_{-0.02}$. The slope is consistent with previous measurements and shallower than the H β R–L relation. The intrinsic scatter of the new R–L relation is substantially smaller than previous studies and comparable to the intrinsic scatter of the H β R–L relation. Our new R–L relation will enable more precise single-epoch mass estimates and SMBH demographic studies at cosmic noon.

Key words: galaxies: nuclei – quasars: general.

1 INTRODUCTION

Accurate mass measurements of supermassive black holes (SMBHs) are critical for understanding their growth over cosmic time. In the local universe, studies have used spatially resolved kinematics of stars or gas at the centres of galaxies to determine the SMBH mass (e.g. Kormendy & Richstone 1995; Gebhardt & Thomas 2009; Barth et al. 2016).However, it is difficult to extend this method to higher redshifts due to the angular resolution limits of current facilities.

The reverberation mapping (RM) technique is a robust method to measure the SMBH mass in active galactic nuclei (AGNs) outside the local universe (Blandford & McKee 1982; Peterson 1993). The AGN broad emission lines vary in response to the stochastic variation of the continuum emission after a time delay due to the light traveltime from the central accretion disc to the broad line region (BLR). The time lag τ is correlated with the SMBH mass through the virial

theorem

$$M_{\mathrm{BH}} = \frac{f c \tau \Delta v^2}{G}, \tag{1}$$

where f is a 'virial factor' determined by the dynamics and structure of the BLR, $R = c\tau$ gives the characteristic BLR size, and Δv is the velocity width of the broad lines. To measure the time lag, RM campaigns generally monitor the target for months to years to obtain the photometric and spectroscopic light curves, which requires substantial observational resources.

An important result of RM studies is a correlation between the BLR radius R and the AGN continuum luminosity L. The existence of an R–L correlation enables a measurement of the SMBH mass from just a single-epoch spectrum. Such single-epoch estimates can be applied to large sample of AGN, making them critical for SMBH demographic studies (e.g. Vestergaard et al. 2008; Kelly & Shen 2013). The R–L relation has been well constrained in nearby AGN using time lag measurements of the H β line (e.g. Kaspi et al. 2000; Bentz et al. 2009, 2013; Grier et al. 2017). However, the H β line

★ E-mail: yu.2231@osu.edu

is not present in optical spectra of higher redshift AGN. At higher redshifts, we need *R–L* relations for other lines, such as Mg II and C IV. Despite previous RM studies of Mg II (e.g. Metzroth, Onken & Peterson 2006; Shen et al. 2016; Lira et al. 2018; Czerny et al. 2019; Homayouni et al. 2020; Zajaček et al. 2020; Yu et al. 2021) and C IV (e.g. Kaspi et al. 2007; Lira et al. 2018; Grier et al. 2019; Hoormann et al. 2019), the *R–L* relations of these lines remain poorly constrained.

Star formation and AGN activity peak at redshifts of $z \sim 1$–2 (e.g. Wolf et al. 2003; Ueda et al. 2014). The single-epoch mass estimates at this epoch of cosmic noon are mainly based on the *R–L* relation of the Mg II line because it is the major broad line observable in optical spectra. Unfortunately, there were less than 10 Mg II lags available until recently (Metzroth et al. 2006; Shen et al. 2016; Lira et al. 2018; Czerny et al. 2019). Therefore, early studies of SMBH demographics generally calibrated the Mg II *R–L* relation to match the H β lags instead of using the direct Mg II lags (e.g. Vestergaard & Osmer 2009). This could lead to a bias because the collisionally excited Mg II line may respond differently to the continuum variability than the photoionized Balmer lines (e.g. Guo et al. 2020). It is therefore critical to better constrain the Mg II *R–L* relation directly with a larger sample of lag measurements.

A promising way to quickly increase the number of lag measurements is through RM campaigns with wide-field multifibre spectrographs and imaging facilities, such as the Sloan Digital Sky Survey (SDSS) RM project (e.g. Shen et al. 2015) and the Dark Energy Survey (DES) – Australian DES (OzDES) RM project (King et al. 2015; Hoormann et al. 2019; Yu et al. 2021). Both surveys have monitored ~800 AGNs at redshifts up to $z \sim 4.5$ for ~5–6 yr. The large sample size and long time duration potentially allow these projects to produce a large number of lag measurements. However, these RM campaigns also face significant challenges, most notably due to the complexity of flux calibrating fibre spectra, the relatively low cadence and signal-to-noise ratio (SNR) of the spectroscopy, and the gaps between observing seasons. As a result, the probability distribution of the lag can be complicated and it is non-trivial to properly select reliable lag measurements and define lag uncertainties.

Homayouni et al. (2020) presented Mg II lags for 57 quasars from the SDSS RM project, from which they identified 24 quasars as their 'gold sample' with the most reliable lags. They derived an Mg II *R–L* relation with a slope of 0.31 and an intrinsic scatter of 0.36 dex from this gold sample. Their *R–L* relation has a shallower slope and larger scatter than the H β relations that typically have a slope of ~0.5 and an intrinsic scatter of ~0.13–0.2 dex (e.g. Bentz et al. 2013; Du et al. 2016). Yu et al. (2021, hereafter Y21) presented nine Mg II lags from the first 5 yr of data on about half of the OzDES RM sample. Their results show much less scatter than Homayouni et al. (2020), but the sample had a small dynamic range in luminosity and therefore could not independently constrain the slope of the *R–L* relation.

Guo et al. (2020) used photoionization models to show that the response of the Mg II line to continuum variability was weaker than the Balmer lines, which could potentially explain the scatter of the Mg II *R–L* relation. However, their model does not quantitatively predict the scatter of the Mg II *R–L* relation. RM studies of the H β line found that AGN with larger Eddington ratios generally had smaller lags at fixed luminosities (e.g. Du et al. 2016, 2018; Dalla Bontà et al. 2020), which may also explain the shallower slope and larger intrinsic scatter of the *R–L* relation when this effect is not included. Martínez-Aldama et al. (2020) reduced the scatter of the Mg II *R–L* relation to ~0.1 dex by including the Eddington ratio as an additional parameter, but their Eddington ratio estimates

depended on the lag measurements. Khadka et al. (2022a) used the ratio $\mathcal{R}_{Fe}$ of the iron line flux to the Mg II line flux as an independent indicator of the Eddington ratio and found that it had no significant impact on the scatter of the Mg II *R–L* relation. A larger Mg II lag sample with a wider redshift and luminosity range is critical for better constraining the Mg II *R–L* relation and understanding its intrinsic scatter.

In this paper, we present 25 Mg II lags from the full OzDES RM sample with 6 yr of data and derive a new Mg II *R–L* relation. Our sample is homogeneously defined through lag quality criteria that are verified by multiple simulations and statistical tests. We describe our observations and spectroscopic analysis in Section 2. Our time series analysis and lag measurements are discussed in Section 3. Section 4 discusses the reliability assessments of the lag measurements. We present the black hole mass and *R–L* relation in Section 5. Section 6 summarizes the paper. This paper adopts a Lambda cold dark matter cosmology with $H_0 = 70$ km s^{-1} Mpc^{-1}, $\Omega_m = 0.3$, and $\Omega_\Lambda = 0.7$.

2 OBSERVATIONS AND SPECTROSCOPIC ANALYSIS

DES is a 6-yr wide-area photometric survey that began in 2013 (Abbott et al. 2018). The survey took images in the *grizY* bands using the Dark Energy Camera (Flaugher et al. 2015) with a 2.2° diameter field of view on the 4-m Victor M. Blanco telescope at the Cerro Tololo Inter-American Observatory. In addition to the 5000-deg² wide-area survey, DES observed 10 supernova (SN) fields approximately every week for the first 5 yr and every three weeks for Y6.

OzDES is a spectroscopic follow-up survey in the DES SN fields, which covers roughly the same time baseline as DES (e.g. Yuan et al. 2015; Childress et al. 2017; Lidman et al. 2020). The spectra cover the wavelength range ~3700–8900 Å and were taken using the AAOmega spectrograph (Smith et al. 2004) with the Two Degree Field (2dF) multifibre positioner (Gray et al. 1993) on the 4-m Anglo-Australian Telescope. The OzDES RM project is one of the key OzDES science projects. Over the six DES observing seasons, it monitored 735 quasars in the DES SN fields with about monthly cadence. An observing season spans about 6 months from July to January. Fig. 1 shows the apparent magnitude and redshift distribution of the OzDES RM quasars. The sample spans an AB magnitude range of $g \sim 17$–23 mag and a redshift range of $z \sim 0.1$–4.5.

We use the pipeline from Hoormann et al. (2019) to calibrate the spectra. The pipeline first calculates the scaling factors from the instrumental flux derived by integrating the extracted and wavelength-calibrated spectra within the DES filters to the DES photometric flux in the *gri* bands. The DES flux is derived from the linear interpolation of the two DES photometric epochs bracketing the spectroscopic epoch. It then fits the scaling factors with a second-order polynomial and generates flux-calibrated spectra by multiplying the polynomial to the extracted and wavelength-calibrated spectra.

The OzDES RM project has developed simulation frameworks for survey design and lag quality assessment (King et al. 2015; Malik et al. 2022; Penton et al. 2022) and published early measurements of continuum lags (Mudd et al. 2018; Yu et al. 2020a), Mg II lags (Y21), and C IV lags (Hoormann et al. 2019) based on the data from the first 4–5 yr. In this paper, we analyse all 6 yr of data for 453 quasars at $0.65 < z < 1.92$. We model and subtract the continuum + iron emission in the rest-frame wavelength region spanning $2260-3050$ Å near the Mg II line (Section 2.1). The redshift range of our candidate sample
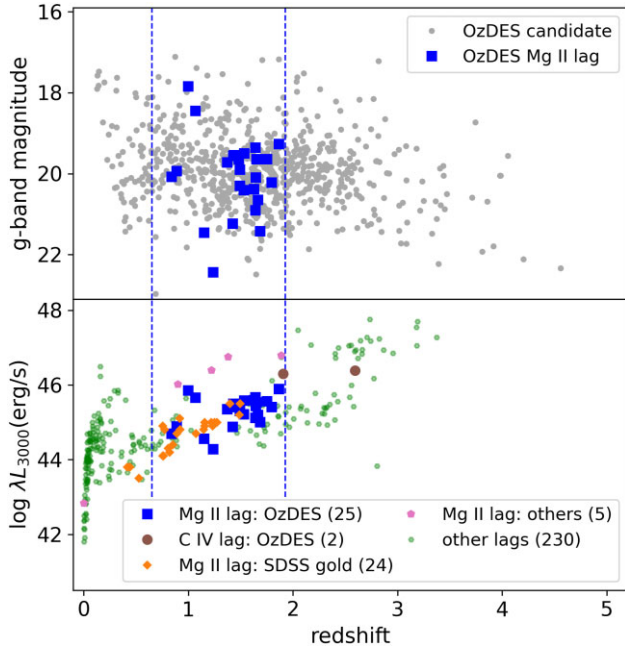
Figure 1. (*Upper panel*) *g*-band apparent magnitude versus redshift of the OzDES RM quasars (grey points) and the subsample that has successful Mg II lag measurements (blue squares). The blue dashed lines show the redshift range of quasars that we analysed in this paper. (*Lower panel*) Monochromatic luminosity at 3000 Å versus redshift. The blue squares, brown points, orange diamonds, pink pentagons, and green hexagons represent the OzDES Mg II lag sample (this work), the OzDES C IV lag sample (Hoormann et al. 2019), the gold sample of the SDSS Mg II lags (Homayouni et al. 2020), other sources with Mg II lags from the literature (Metzroth et al. 2006; Lira et al. 2018; Czerny et al. 2019; Zajaček et al. 2020, 2021), and other RM sources from the literature (Peterson et al. 2004, 2005; Kaspi et al. 2007; Bentz et al. 2009, 2013, 2014, 2016; Denney et al. 2010; Barth et al. 2011a, b, 2013; Grier et al. 2012, 2017, 2019; Du et al. 2014, 2015, 2016, 2018; Pei et al. 2014; Trevese et al. 2014; Wang et al. 2014; Lu et al. 2016; Fausnaugh et al. 2017; Lira et al. 2018; Zhang et al. 2019; Hu et al. 2021; Li et al. 2021; Williams et al. 2021; Vivian et al. 2022), respectively. The number of lags in each sample is given in the brackets. We converted the monochromatic luminosities at 5100 and 1350 Å to 3000 Å using the bolometric corrections from Richards et al. (2006).

ensures that the iron fitting range is fully covered by the OzDES spectra. The spectroscopic calibration could introduce correlated errors between the spectral pixels over a wide wavelength range. We estimate the calibration uncertainties based on the F stars monitored by OzDES (Section 2.2).

2.1 Continuum and iron subtraction

A challenge in analysing the Mg II line is the strong contribution from nearby iron emission lines (e.g. Wills et al. 1980; Wills, Netzer & Wills 1985; Verner et al. 1999). The iron lines could also have reverberation signals that contaminate the Mg II lag signal (e.g. Barth et al. 2013). We fit and subtract the continuum + iron emission and derive the Mg II line flux using the pipeline from Y21. Our model

$$f_{\text{model}}(\lambda) = f_{\text{c}}(\lambda) + f_{\text{Fe}}(\lambda) \tag{2}$$

consists of a power-law continuum

$$f_{\text{c}}(\lambda) = A_{\text{c}}(\lambda/\lambda_0)^{\alpha}, \tag{3}$$

with an index α and a normalization A_{c} at $\lambda_0 = 2599$ Å,[1] and an iron emission line component

$$f_{\text{Fe}}(\lambda) = A_{\text{t}} f_{\text{t}}(\lambda) * G(w) \tag{4}$$

modelled by an iron template $f_{\text{t}}(\lambda)$ of a normalization A_{t} convolved with a Gaussian kernel $G(w)$ of a width w to account for the velocity broadening of the BLR. The four free parameters of the model are A_{c}, α, A_{t}, and w.

We adopt the empirical iron template from Vestergaard & Wilkes (2001) based on the Seyfert galaxy I Zwicky 1. While the Vestergaard & Wilkes (2001) template did not model the iron emission under the Mg II line, Y21 tested other iron templates by Tsuzuki et al. (2006) and Salviander et al. (2007) that modelled the iron emission under Mg II and found that the choice of iron template had little impact on the lag measurements. We fit the spectra over the rest-frame wavelength ranges 2260–2690 and 2910–3050 Å using a Markov chain Monte Carlo (MCMC) sampler. We do not include the wavelength range near the Mg II line, since it is difficult to distinguish the iron emission from the strong Mg II line within this range. Using a wider fitting range has little impact on our lag measurements. When fitting the single-epoch spectra, we cannot constrain the broadening width w very well due to the low SNR, so we fix it to the best-fitting value found for the co-added spectra. While the width of the iron lines could vary in response to the continuum variability (e.g. Korista & Goad 2004; Guo et al. 2020; Wang et al. 2020), Y21 found that such variability had little impact on the derived Mg II line flux. We do not include Balmer continuum in the fitting. Based on the simulations in Lawther et al. (2018), we estimate that the variability of the Balmer continuum under the Mg II line is much smaller than the uncertainty of the Mg II flux. Therefore, the Balmer continuum will not have significant impact on our lag measurements.

We derive the Mg II flux as $F_{\text{line}} = F_{\text{total}} - F_{\text{model}}$, where F_{total} is the integrated spectral flux over the rest-frame wavelength range 2700–2900 Å before continuum and iron subtraction and F_{model} is the integrated continuum + iron model flux. The line flux uncertainty is estimated as

$$\sigma_{\text{line}}^2 = \sigma_{\text{total}}^2 + \sigma_{\text{model}}^2, \tag{5}$$

where

$$\sigma_{\text{total}} = \sqrt{\sum_i \sigma_{\text{total},i}^2} \, \Delta\lambda \tag{6}$$

is the uncertainty in the total flux F_{total}, $\sigma_{\text{total},i}$ is the uncertainty of the ith pixel, $\Delta\lambda$ is the wavelength pixel size, and σ_{model} is the uncertainty in the model flux F_{model}. We estimate σ_{model} as the scatter of the model fluxes in the MCMC chain. Fig. 2 shows an example of the continuum + iron modelling. The model generally matches the observed spectra well. We visually inspect all spectra and exclude epochs from further analysis where the best-fitting model fails to match the spectra or where the spectra are contaminated by instrumental artefacts, such as the bump at ∼7100 Å created by a light-emitting diode (LED) in the 2dF gripper gantry. Figures for all spectra of our final sample of quasars are available in the supplementary material.

---

[1]The constant λ_0 is chosen to reduce the error correlation between the power-law index α and normalization A_{c} by reducing the non-diagonal terms of the Fisher matrix.
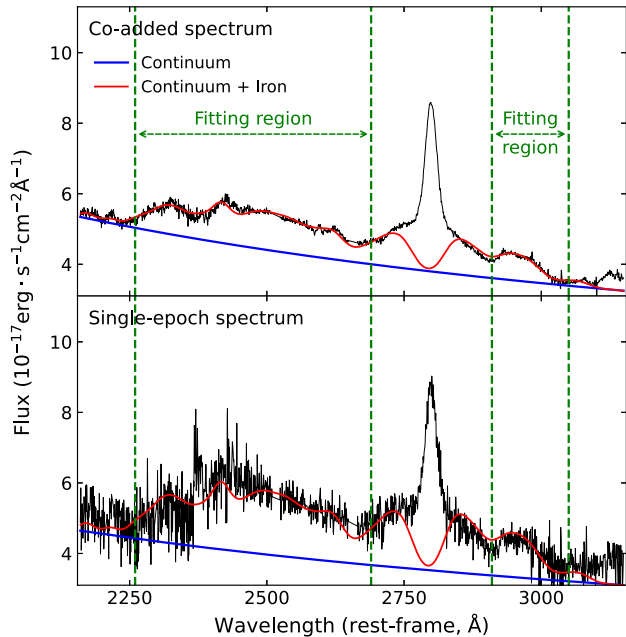
Figure 2. Examples of the continuum + iron modelling of the co-added spectrum (upper panel) and a single-epoch spectrum (lower panel) in the rest frame of DES J003052.76−430301.08. The green dashed lines show the regions where we fit the spectra. The blue and red solid lines are the best-fitting continuum and continuum + iron models, respectively.

2.2 Calibration uncertainty

We estimate the calibration uncertainty and propagate it to the error budget of the Mg II line flux using the pipeline from Y21 based on the F stars observed by OzDES in each epoch. For each F star, we calculate the mean $\langle f_{*,i} \rangle$ and rms $S_{*,i}$ of the calibrated spectra over all epochs, where i corresponds to the ith pixel. Since F stars do not have intrinsic variability, the residual variation $S_{*,i}$ is due to a combination of the mostly uncorrelated photon noise and the correlated calibration uncertainty. We cannot directly derive the calibration uncertainty from $S_{*,i}$ since it is dominated by the photon noise at the pixel level. We therefore bin the spectra by 300 Å to suppress the photon noise, while the correlated calibration uncertainty remains. The residual variation of the binned spectra is an estimate of the calibration uncertainty.

We propagate the calibration uncertainty to the line flux uncertainty using a Monte Carlo method. We define a 'warping function'

$$W_{bj} = f_{*,bj}/\langle f_{*,b}\rangle, \tag{7}$$

where $f_{*,bj}$ is the flux of the binned F-star spectra in the bth bin of the jth epoch and $\langle f_{*,b}\rangle$ is the mean of the binned spectra over all epochs. We then derive a continuous warping function $W_j(\lambda)$ by interpolating the discrete function W_{bj} with a third-order spline function. Each epoch of the F-star spectra provides a warping function $W_j(\lambda)$, and each warping function is a realization of the spectral variability due to the calibration uncertainty. We create 2343 warping functions based on 161 F stars. This provides a 'library' of warping functions for each spectroscopic epoch. Multiplying the quasar spectrum with the warping functions of the corresponding epoch gives realizations of the quasar spectra warped by the calibration uncertainty. In each warped spectra, we calculate the Mg II flux using the method described in Section 2.1. We then multiply the fractional variation of the warped Mg II fluxes by the Mg II flux of the observed spectra to derive the line flux uncertainty contributed by the calibration

procedure. This uncertainty is added in quadrature to the line flux uncertainty estimated in Section 2.1. The median calibration uncertainty is ∼4 per cent.

The calibration pipeline uses the linear interpolation of the two neighbouring DES epochs to estimate the continuum flux at a spectroscopic epoch, which is a reasonable estimate since the cadence of the DES photometric light curve is much higher than the OzDES spectroscopy. While the photometric cadence in Y6 is lower than the first 5 yr, the Y6 spectra are generally taken within a few days of the neighbouring photometric epochs. The only cases where the linear interpolation can significantly increase the calibration uncertainty are two spectroscopic epochs taken at 2018 June 15 (MJD 58284) and 2018 June 24 (MJD 58293) for some quasars. They are in the seasonal gap between DES Y5 and Y6 and therefore have no nearby photometric epoch. This introduces additional calibration error due to the large uncertainty of the continuum flux. In these two cases, we interpolate the photometric light curve with a damped random walk (DRW) stochastic process and calculate the fractional uncertainty of the DRW model at the time of the spectroscopic epoch. This characterizes the uncertainty in the overall normalization of the calibration and we add it as an additional uncertainty to the error budget of the Mg II line flux. The additional uncertainty is ∼10 per cent for these two cases.

3 TIME SERIES ANALYSIS

We use the g-band photometry from the DES data base for the continuum light curves and the pipeline described above to create Mg II line light curves. Machine-readable light curves for our final sample are available in the supplementary material. We use JAVELIN (e.g. Zu, Kochanek & Peterson 2011; Zu et al. 2013) and the interpolated cross-correlation function (ICCF; e.g. Gaskell & Peterson 1987; Peterson et al. 1998, 2004) method to measure the time lags. JAVELIN uses a DRW stochastic process to interpolate the light curve and assumes that the line light curve is the continuum light curve convolved with a top-hat transfer function. JAVELIN fits the continuum and line light curves simultaneously with an MCMC sampler to derive the posterior probability distributions of the amplitude σ_{drw} and characteristic time-scale τ_{drw} of the DRW model, the scale s_l and width w_l of the transfer function, and the mean time lag τ. The algorithm sets the prior of the DRW parameters σ_{drw} and τ_{drw} as their posterior distributions from fitting only the continuum light curve. We use a flat prior for the time lag τ within $[\tau_{min}, \tau_{max}]$ d, while we allow the other parameters to vary freely.

We use PYCCF (Sun, Grier & Peterson 2018), a PYTHON implementation of the ICCF method. This method linearly interpolates the light curves and calculates the cross-correlation function (CCF) within a lag range $[\tau_{min}, \tau_{max}]$ d. It then uses the range of the CCF where the cross-correlation coefficient is at least 80 per cent of the maximum and estimates the lag as its centroid or peak. For the lag uncertainty, it first creates light-curve realizations by randomizing the single-epoch flux by its uncertainty and randomly subsampling the epochs with replacement. It then calculates the centroid and peak of the CCF for each realization to create the cross-correlation centre distribution (CCCD) and cross-correlation peak distribution (CCPD). The scatter of these distributions gives the lag uncertainty estimate. We generate 8000 realizations and adopt the realizations with $r_{peak} > 0.5$ to create the CCCD and CCPD, where the r_{peak} is the peak value of the CCF. We use CCCD as the fiducial lag probability distribution of the ICCF method, since previous work found that it provided better lag estimates than CCPD (e.g. Peterson et al. 2004).

The lag distributions from JAVELIN and ICCF usually have multiple peaks that are mostly due to the aliasing effects caused by the seasonal gaps, so it is non-trivial to identify successful lag measurements and estimate their uncertainties. We use two different methods to analyse the lag distributions, leading to two sets of criteria to select successful lag measurements.

3.1 Symmetric prior

Method 1 resembles the lag analysis in Y21 and the SDSS RM project (e.g. Grier et al. 2019; Homayouni et al. 2020). We set a lag prior range [$\tau_{min} = -1000$ d, $\tau_{max} = 1000$ d] for both JAVELIN and ICCF and define a weighting function to suppress aliasing. The weighting function is the convolution of two components. The first component is defined as

$$P(\tau) = [N(\tau)/N(0)]^2, \tag{8}$$

where $N(\tau)$ is the number of overlapping points between the continuum light curve shifted by the time lag τ and the line light curve. This penalizes lags in the seasonal gaps where the shifted continuum has little overlap with the line light curve. The second component is the autocorrelation function (ACF) of the continuum light curve, which characterizes how fast the continuum varies. We set ACF = 0 when it is below zero.

We multiply the lag distribution by the weighting function and convolve the weighted distribution with a Gaussian kernel that has a width of 12 d, the same width used in Y21 and Homayouni et al. (2020). We define the major peak as the highest peak in the weighted and smoothed lag distribution. When there are multiple connected peaks, we define one as a separate peak if its prominence exceeds 10 per cent of the prominence of the neighbouring peaks and it is separated from the neighbouring peaks by at least 10 d. We use the package `scipy.signal.peak_prominences` (Jones et al. 2001) to calculate the peak prominence defined as the vertical distance between the peak and the higher minimum at its two sides. We then define the lag as the median of the unweighted lag distribution within the major peak and define the lag uncertainty based on its 16th and 84th percentiles.

We define the first set of selection criteria based on Method 1:

(i) $f_{peak} > 0.6$ for the JAVELIN lag distribution, where f_{peak} is the probability within the major peak.
(ii) The lag uncertainty from JAVELIN is less than 110 d.
(iii) The lags from JAVELIN and ICCF agree within 2σ.

The first criterion ensures that the major peak has enough significance to be distinguished from the aliasing peaks. The second criterion requires that the lag distribution has enough constraining power and excludes lag distributions that are flat over a wide range of lags. The agreement between JAVELIN and ICCF required by the third criterion helps to increase the lag reliability. We obtain 62 lags that pass the Method 1 criteria, 48 of which are positive.

3.2 Positive prior

Method 2 is defined by Penton et al. (2022) and is based on simulated light curves that have the same cadence and SNR as the OzDES observations. We use a lag prior range [$\tau_{min} = 0$ d, $\tau_{max} = 1000$ d] to derive the lag distribution from JAVELIN and ICCF. We analyse the full lag distribution binned by 3 d without any weighting or major peak identification. We define the second set of selection criteria based on Method 2:

(i) The mean absolute deviation of the JAVELIN lag distribution is less than 110 d.
(ii) The separation between the median and peak of the JAVELIN lag distribution is less than 110 d.
(iii) The separation between the peaks of the JAVELIN and ICCF lag distributions is less than 100 d.

The threshold values in each criterion are the same as Penton et al. (2022). The first and second criteria effectively require the lag distribution to have a strong major peak compared to the aliasing peaks, since the aliasing peaks would increase the mean absolute deviation and result in a difference between the median and peak. There are 56 quasars that pass the Method 2 criteria.

3.3 Final measurements

We define a successful lag measurement as one that passes both the Method 1 and 2 criteria. This yields 25 lag measurements, which we refer to as our final sample. We adopt the lag and uncertainty estimates in Section 3.1 based on the JAVELIN lag distributions, since previous studies showed that JAVELIN provides better lag and uncertainty estimates than the ICCF method (e.g. Li et al. 2019; Yu et al. 2020b). Table 1 gives the lag measurements of the final sample. The final sample spans a redshift range of $0.84 \leq z \leq 1.86$ and an observed lag range of 130 d $< \tau < 880$ d.

Table 2 gives two metrics of the light-curve variability of the final sample. The first metric is the fractional variability F_{var} (e.g. Rodríguez-Pascual et al. 1997; Vaughan et al. 2003) defined as

$$F_{var} = \frac{\sqrt{S^2 - \langle\sigma^2\rangle}}{\langle F\rangle}, \tag{9a}$$

$$\sigma_{F_{var}} = \sqrt{\left(\sqrt{\frac{1}{2N}}\frac{\langle\sigma^2\rangle}{F_{var}\langle F\rangle^2}\right)^2 + \left(\sqrt{\frac{\langle\sigma^2\rangle}{N}}\frac{1}{\langle F\rangle}\right)^2}, \tag{9b}$$

where S is the standard deviation of the light curve, $\langle\sigma^2\rangle$ is the mean square of the flux uncertainties, $\langle F\rangle$ is the mean flux, $\sigma_{F_{var}}$ is the uncertainty of F_{var}, and N is the number of epochs. The second metric χ_r^2 is defined as

$$\chi^2 = \sum_i \frac{(F_i - \langle F\rangle)^2}{\sigma_i^2}, \tag{10a}$$

$$\chi_r^2 = \chi^2/(N-1), \tag{10b}$$

where F_i and σ_i are the flux and uncertainty of the ith epoch, respectively. The fractional variability F_{var} characterizes the excess variability amplitude relative to the mean flux, while χ_r^2 characterizes the significance of the variability relative to the uncertainties.

Fig. 3 shows examples of the light curves and lag distributions of our final sample. The lag distributions exhibit clear major peaks. The major peaks are significantly stronger than the secondary peaks for the JAVELIN lag distributions. The median JAVELIN major peak fraction f_{peak} of the final sample is 0.78. The lags from the symmetric and positive prior ranges all agree within 1σ. The JAVELIN and ICCF lags are all consistent within 100 d and within 2σ, as required by the selection criteria.

The light curves in Fig. 3 exhibit clear variability features. The black points in the lower left panels show the continuum light curve shifted by the best-fitting JAVELIN lag with the symmetric prior range. For the sources shown in the top two rows, the shifted continuum light curve matches the line light curve well, which supports the reliability of the lag measurement. The lag of the third source is close to the 1.5-yr seasonal gap, but its shifted continuum light curve is a reasonable 'interpolation' between the line light curves in different seasons.

Table 1. Characteristics of the 25 AGNs in our final sample with successful Mg II lag measurements. Columns (1) and (2) give the DES name and redshift of the source. Columns (3) and (4) give the lags and uncertainties in the observer frame from JAVELIN and the ICCF method, respectively. Column (5) gives the probability within the major peak of the JAVELIN lag distribution (see Section 3.1). Column (6) gives the false positive rate from simulations (see Section 4.1). Column (7) gives the spectral flux density and its uncertainty at 3000 Å in unit of 10^{-17} erg s^{-1} cm^{-2} Å^{-1}. Column (8) gives the 3000-Å monochromatic luminosity and its uncertainty. Column (9) gives the ratio $\mathcal{R}_{Fe}$ of the iron flux to the Mg II flux (see Section 5.1). Columns (10) and (11) give the line dispersion and black hole mass. The black hole mass uncertainty is about 0.4 dex.

Source name	z	τ_{JAV} (d)	τ_{ICCF} (d)	f_{peak}	FPR (per cent)	f_{3000} (see caption)	$\log[\lambda L_{3000}$ (erg s^{-1})]	$\mathcal{R}_{Fe}$	σ_{line} (km s^{-1})	$\log(M_{BH}/M_\odot)$
DES J024340.09+001749.40	1.44	818^{+39}_{-6}	797^{+54}_{-20}	0.76	7.9	2.75 ± 0.15	45.41 ± 0.02	1.44 ± 0.17	3181.0	9.46
DES J025254.18+001119.70	1.64	415^{+27}_{-166}	420^{+27}_{-44}	0.75	3.7	0.93 ± 0.02	45.12 ± 0.01	1.26 ± 0.11	2435.4	8.89
DES J024831.08+005025.60	0.89	286^{+36}_{-102}	341^{+103}_{-85}	0.91	0.0	3.52 ± 0.15	44.89 ± 0.02	1.78 ± 0.23	2130.3	8.76
DES J024723.54+002536.50	1.86	867^{+64}_{-66}	880^{+44}_{-30}	0.84	0.0	3.73 ± 0.10	45.89 ± 0.01	3.68 ± 0.28	2452.6	9.19
DES J024944.09+003317.50	1.48	412^{+31}_{-67}	402^{+66}_{-39}	0.88	10.0	3.10 ± 0.06	45.50 ± 0.01	1.48 ± 0.12	2207.4	8.83
DES J024455.45−011500.40	1.53	165^{+28}_{-21}	210^{+89}_{-39}	0.77	8.0	1.47 ± 0.05	45.22 ± 0.02	1.93 ± 0.29	3731.1	8.88
DES J025225.52+003405.90	1.62	520^{+31}_{-26}	505^{+43}_{-39}	0.69	0.0	2.86 ± 0.06	45.59 ± 0.01	1.93 ± 0.18	2637.9	9.06
DES J022716.52−050008.30	1.64	524^{+14}_{-14}	495^{+52}_{-49}	0.68	2.1	1.94 ± 0.06	45.44 ± 0.01	1.45 ± 0.15	2128.2	8.88
DES J022751.50−044252.70	1.79	538^{+28}_{-13}	558^{+33}_{-33}	0.70	0.0	1.38 ± 0.05	45.41 ± 0.02	1.75 ± 0.18	2849.7	9.12
DES J022208.15−065550.50	1.66	439^{+25}_{-31}	423^{+37}_{-40}	0.96	11.5	1.09 ± 0.03	45.20 ± 0.01	1.90 ± 0.38	2167.8	8.81
DES J033836.19−295113.50	1.15	225^{+46}_{-51}	280^{+85}_{-49}	0.96	0.0	0.78 ± 0.04	44.57 ± 0.02	2.55 ± 0.38	2987.0	8.90
DES J033903.66−293326.50	1.68	308^{+40}_{-66}	284^{+86}_{-30}	0.67	10.0	0.67 ± 0.02	45.01 ± 0.01	1.64 ± 0.15	3229.6	9.00
DES J033328.93−275641.21	0.84	175^{+16}_{-17}	182^{+35}_{-69}	0.82	2.3	2.70 ± 0.22	44.70 ± 0.04	1.59 ± 0.16	2549.0	8.72
DES J022436.64−063255.90	1.42	181^{+25}_{-26}	147^{+48}_{-44}	0.83	0.0	0.83 ± 0.03	44.88 ± 0.02	1.36 ± 0.18	3308.3	8.84
DES J033211.42−284323.99	1.24	132^{+27}_{-21}	137^{+69}_{-78}	1.00	14.3	0.32 ± 0.03	44.28 ± 0.04	1.13 ± 0.19	3388.9	8.75
DES J033213.36−283620.99	1.49	171^{+13}_{-11}	192^{+31}_{-45}	0.85	3.6	2.23 ± 0.04	45.37 ± 0.01	1.23 ± 0.10	2775.1	8.65
DES J003710.86−444048.11	1.07	382^{+34}_{-30}	430^{+29}_{-35}	0.93	12.0	12.18 ± 0.20	45.67 ± 0.01	1.79 ± 0.04	2398.1	8.95
DES J003922.97−430230.41	1.37	564^{+53}_{-34}	637^{+17}_{-41}	0.76	17.2	2.80 ± 0.07	45.35 ± 0.01	1.32 ± 0.09	2416.8	9.10
DES J002933.85−435240.69	1.00	571^{+13}_{-29}	540^{+32}_{-32}	0.73	18.2	23.20 ± 0.26	45.86 ± 0.00	1.19 ± 0.07	2257.1	9.09
DES J003207.44−433049.00	1.53	376^{+10}_{-5}	362^{+21}_{-34}	0.65	3.0	3.40 ± 0.03	45.59 ± 0.00	2.06 ± 0.07	1901.2	8.65
DES J003015.00−430333.52	1.65	508^{+30}_{-25}	467^{+28}_{-19}	0.73	2.6	2.40 ± 0.04	45.54 ± 0.01	1.16 ± 0.04	3915.7	9.39
DES J003052.76−430301.08	1.43	383^{+35}_{-14}	388^{+35}_{-37}	0.78	5.3	3.46 ± 0.04	45.50 ± 0.00	1.93 ± 0.08	2117.0	8.77
DES J003232.61−433302.99	1.49	537^{+11}_{-14}	535^{+43}_{-57}	0.98	0.0	1.95 ± 0.05	45.31 ± 0.01	2.03 ± 0.08	3927.3	9.45
DES J003234.33−431937.81	1.64	656^{+63}_{-31}	649^{+13}_{-16}	0.71	0.0	3.36 ± 0.04	45.67 ± 0.01	1.72 ± 0.09	1784.6	8.82
DES J003206.50−425325.22	1.75	479^{+40}_{-26}	466^{+26}_{-26}	0.95	0.0	2.16 ± 0.06	45.57 ± 0.01	1.49 ± 0.07	3769.7	9.32

A special feature of DES J003206.50−425325.22 (bottom panel of Fig. 3) is the two outliers at MJD 58073 and 58399. The excess flux is due to a significant broadening of the Mg II line. This can be intrinsic to the Mg II line or due to a drastic change in the iron emission that is not characterized by the model. The JAVELIN lag distribution would be dominated by a sharp aliasing peak at ∼540 d if we included these two epochs, which differs from the ∼470-d ICCF lag. For lags of a few hundred days, we expect the signal to come from light-curve features over several years rather than dramatic short time-scale variability, so we exclude these two epochs for this particular source. Excluding these two epochs also gives a cleaner JAVELIN lag distribution compared to the Y5 results where we kept the MJD 58073 epoch, and the best-fitting lag changes by ∼40 d relative to Y5.

Seven of the nine quasars from Y21 pass our final sample criteria in this paper after adding the Y6 data. The black dashed lines in the top and bottom panels of Fig. 3 show the lag distributions presented in Y21 based on the first 5-yr light curves. The new and old lags agree within 1σ except for the case of DES J003206.50−425325.22 discussed above. Adding the Y6 data suppresses some aliasing peaks and makes the lag signal cleaner. Two quasars from Y21 (DES

J021612.83−044634.10 and DES J033553.51−275044.70) fail to pass the lag selection. While both pass the Method 1 criteria, they are excluded by the Method 2 criteria due to large mean absolute deviations and differences between the JAVELIN and ICCF lags caused by aliasing peaks.

4 LAG RELIABILITY

We assess the reliability of lag measurements using simulations based on both the DRW model and the observed light curves of intensively monitored local AGN. We then discuss the lag reliability of our final sample and compare with the samples selected by only one of the criteria.

4.1 Simulations with DRW

We adopt the simulation tool developed by Penton et al. (2022) to create simulated light curves following the same procedure as Y21. For each of the 25 final sample sources that pass both sets of criteria for Method 1 and 2, we create 1000 realizations of DRW light curves that have the same variability as the observed continuum light

Table 2. Light-curve variability of the final sample. Column (1) gives DES name of the source. Columns (2) and (3) give the fractional variability $F_{\rm var}$ defined by equation (9) of the g-band and Mg II light curves, respectively. Columns (4) and (5) give the $\chi_{\rm r}^2$ value defined by equation (10).

Source name	$F_{\rm var}$ (g band)	$F_{\rm var}$ (Mg II)	$\chi_{\rm r}^2$ (g band)	$\chi_{\rm r}^2$ (Mg II)
DES J024340.09+001749.40	0.252 ± 0.001	0.121 ± 0.013	164 650.0	6.6
DES J025254.18+001119.70	0.141 ± 0.002	0.117 ± 0.041	128.8	3.0
DES J024831.08+005025.60	0.196 ± 0.002	0.186 ± 0.025	240.2	4.8
DES J024723.54+002536.50	0.175 ± 0.001	0.228 ± 0.029	577.2	4.2
DES J024944.09+003317.50	0.113 ± 0.001	0.120 ± 0.022	3308.1	4.2
DES J024455.45−011500.40	0.205 ± 0.002	0.207 ± 0.017	485.3	7.0
DES J025225.52+003405.90	0.120 ± 0.002	0.111 ± 0.019	46.4	3.4
DES J022716.52−050008.30	0.217 ± 0.001	0.114 ± 0.012	3477.1	5.0
DES J022751.50−044252.70	0.199 ± 0.001	0.244 ± 0.016	23 298.1	7.5
DES J022208.15−065550.50	0.128 ± 0.002	0.213 ± 0.044	62.5	4.4
DES J033836.19−295113.50	0.222 ± 0.005	0.296 ± 0.023	54.6	8.3
DES J033903.66−293326.50	0.161 ± 0.004	0.185 ± 0.037	35.8	2.7
DES J033328.93−275641.21	0.305 ± 0.003	0.140 ± 0.016	281 561.2	7.0
DES J022436.64−063255.90	0.263 ± 0.003	0.098 ± 0.026	321.5	3.8
DES J033211.42−284323.99	0.311 ± 0.006	0.244 ± 0.023	94.9	8.9
DES J033213.36−283620.99	0.177 ± 0.001	0.163 ± 0.015	5525.8	6.1
DES J003710.86−444048.11	0.084 ± 0.001	0.084 ± 0.009	158 385.6	5.2
DES J003922.97−430230.41	0.160 ± 0.001	0.140 ± 0.019	1995.1	3.2
DES J002933.85−435240.69	0.073 ± 0.001	0.174 ± 0.020	2608.0	3.9
DES J003207.44−433049.00	0.096 ± 0.001	0.102 ± 0.015	127.4	3.4
DES J003015.00−430333.52	0.078 ± 0.002	0.046 ± 0.005	219.0	4.3
DES J003052.76−430301.08	0.085 ± 0.001	0.049 ± 0.008	662.2	2.8
DES J003232.61−433302.99	0.251 ± 0.002	0.086 ± 0.008	405.7	4.7
DES J003234.33−431937.81	0.070 ± 0.002	0.075 ± 0.018	63.4	1.8
DES J003206.50−425325.22	0.172 ± 0.001	0.206 ± 0.013	243.3	6.8

curve. We use the DRW light curve as the simulated continuum and convolve it with a top-hat transfer function to create the simulated line light curves. The input lag $\tau_{\rm i}$ of the transfer function is randomly drawn from a uniform distribution between 10 and 1000 d. We then resample and add noise to the simulated light curves so that their cadence and SNR match the observed light curves.

We then use the method described in Section 3 to measure lags from the simulated light-curve pairs. We define a lag as a 'false positive' if the measured lag $\tau_{\rm m}$ differs from the the input lag $\tau_{\rm i}$ by 3σ. For a final sample source with an observed lag $\tau_{\rm obs}$, we define the false positive rate (FPR) as

$$\text{FPR} = N_{\rm bad,m}(\tau_{\rm obs})/N_{\rm p,m}(\tau_{\rm obs}), \tag{11}$$

where $N_{\rm p,m}(\tau_{\rm obs})$ is the number of realizations where the measured lag $\tau_{\rm m}$ passes the final sample selection and is within 1σ of $\tau_{\rm obs}$, and $N_{\rm bad,m}(\tau_{\rm obs})$ is the number of false positives among the $N_{\rm p,m}(\tau_{\rm obs})$ realizations. The FPR is an estimate of the probability that the observed lag $\tau_{\rm obs}$ is different from the true lag. Table 1 gives the FPR of each AGN in the final sample. The filled histograms in Fig. 4 show the FPR distribution of the final sample. The median FPR is $\sim$3 per cent. The sum of the FPR for all 25 AGNs is $\sim$1.3, which indicates that there could be one incorrect lag in the sample. The median and average of the FPR are similar to the Y21 sample where the median was $\sim$4 per cent and the sum was 0.44 for nine AGNs.

4.2 Simulations with reference light curves

The simulations in Section 4.1 assume that the AGN variability is a DRW stochastic process and that the line light curve is related to the continuum light curve by a top-hat transfer function. These assumptions may not hold in real AGN. For example, the AGN

variability could deviate from the DRW model on time-scales below $\sim$ month (e.g. Mushotzky et al. 2011; Kasliwal et al. 2015; Smith et al. 2018). AGN could also have 'BLR holidays' when the broad line variability is not correlated with the continuum variability (e.g. Goad et al. 2016; Horne et al. 2021), and this could hamper the lag recovery (Yu et al. 2020b).

We perform additional simulations using the observed light curves of several intensively monitored local AGNs as 'reference light curves'. We first scale the time axis of the reference light curve by a factor of X_t so that its baseline length matches the 6-yr baseline of the OzDES continuum and line light curves. While scaling the baseline increases the variability time-scale, Stone et al. (2022) found that the DRW time-scale $\tau_{\rm drw}$ of AGN could span $\sim$1.5 orders of magnitude, so the scaling does not make the variability time-scale unrealistic for AGN. We then shift the scaled reference light curve of the emission line by $\Delta t = \tau_{\rm i} - X_t \tau_{\rm ref}$ so that the lag between the shifted, scaled reference light curves of the continuum and emission line equal the desired input lag $\tau_{\rm i}$, where $\tau_{\rm ref}$ is the lag between original reference light curves from the literature. The second row of Fig. 5 shows an example of the scaled reference light curves.

We interpolate the scaled reference continuum and line light curves using the predicted light curves from JAVELIN (red solid line in Fig. 5) and resample them to the same cadence as the OzDES light curves (top row of Fig. 5) to create the simulated light curves. We then assign an uncertainty $\sigma_{\rm sim,j} = K\sigma_{\rm oz,j}$ to each simulated epoch, where j corresponds to the jth epoch, K is a constant coefficient, and $\sigma_{\rm oz,j}$ is the uncertainty of the corresponding OzDES epoch. The constant K is derived such that the variability

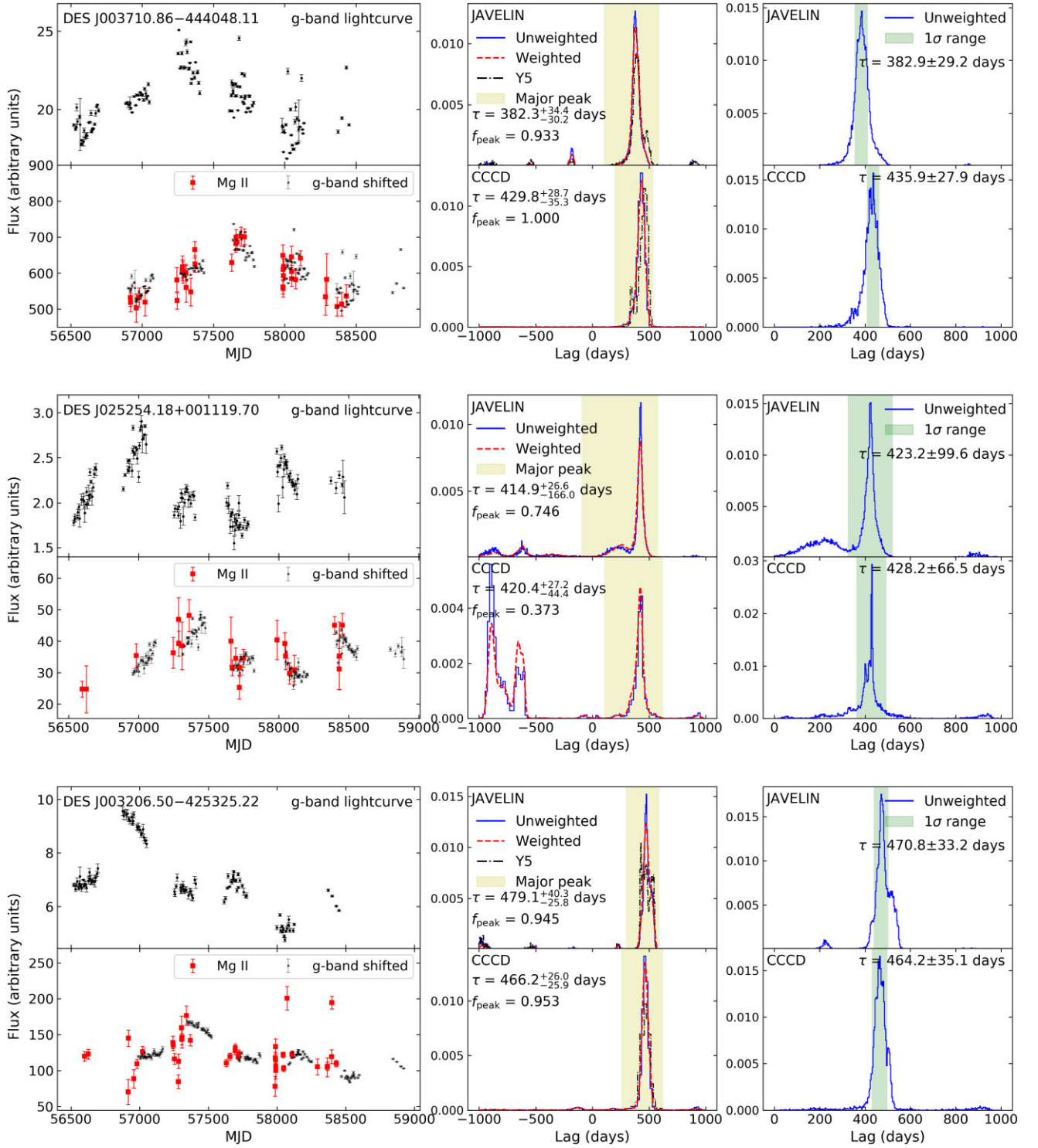$$\chi_{\rm var}^2 = \sum_j \frac{(f_j - \langle f \rangle)^2}{\sigma_j^2} \tag{12}$$

Figure 3. Light curves and lag measurements. Each of the three main rows is for an AGN with its name given in the upper left corner. (*Left column*) The upper and lower panels show the *g*-band light curve and the Mg II line light curve, respectively. The black points in the lower panel show the *g*-band light curve shifted by the best-fitting lag. (*Middle column*) The upper and lower panels show the lag distributions from JAVELIN and ICCF with a symmetric lag prior. The blue solid and red dashed lines represent the unweighted and weighted lag distributions, respectively. For sources presented in Y21, the black dash–dotted lines show the lag distributions from the 5-yr light curves. The yellow shaded area marks the major peak region. (*Right column*) Lag distributions with a positive lag prior. The green shaded area represents the 1σ range centred at the peak, where σ is defined as the mean absolute deviation of the lag distribution.
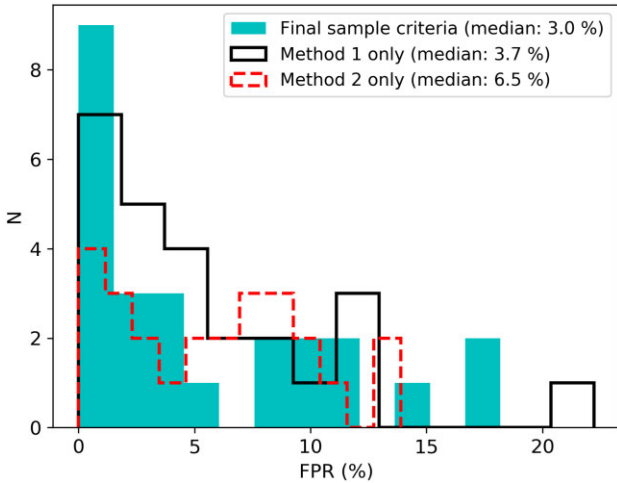
Figure 4. FPR distribution of the final sample. The cyan filled histograms are from simulations where the lag quality criteria are same as the final sample (Method 1 + 2). The black solid and red dashed lines are from simulations where we only use the Method 1 criteria or the Method 2 criteria to select successful lag measurements, respectively.

of the simulated light curve equals that of the OzDES light curve, where f_j and σ_j are the flux and uncertainty of the jth epoch, respectively, and $\langle f \rangle$ is the mean flux. If the assigned uncertainty $\sigma_{\mathrm{sim},j}$ is larger than the original uncertainty $\sigma_{0,j}$ of the reference light curve, we add additional Gaussian noise with a variance of $\sigma_{\mathrm{sim},j}^2 - \sigma_{0,j}^2$ to the simulated epoch. We do not add additional noise when $\sigma_{\mathrm{sim},j} < \sigma_{0,j}$, so some simulated light curve may have underestimated noise relative to the observed light curves. This will lead to an underestimate of the lag uncertainty from the simulated light curves and an overestimate of the FPR. It is not a significant problem for our purpose, since it puts an even higher requirement on the lag quality. While matching the overall variability of the light curves does not guarantee that the short time-scale variability is identical, we expect the major lag signal to be from light-curve features over multiple years, so this approximation would not significantly affect our simulation results. The third row of Fig. 5 shows an example of a final simulated light curve.

Each reference AGN effectively gives a realization of the simulated light curve. We use 12 reference AGNs summarized in Table 3 from Grier et al. (2012), Du et al. (2014), Wang et al. (2014), and De Rosa et al. (2015, 2018) where the cadences of the scaled reference light curves are higher than 15 and 20 d for the continuum and emission line, respectively. All but Mrk 382 have velocity-resolved RM results (Grier et al. 2013a; De Rosa et al. 2018; Li et al. 2018; Horne et al. 2021). NGC 5548 has light curves for two different seasons, which we use as separate reference light curves, so there are in total 13 realizations of simulated light curves. For each realization, we use two different sets of input lag, cadence, and variability: $\tau_i = 370.1$ d that mimics the OzDES light curves of DES J003207.44−433049.00 and $\tau_i = 540.8$ d that mimics the OzDES light curves of DES J003232.61−433302.99. These input lags characterize two regimes of lag measurements where the shifted continuum overlaps well with the line light curve and where much of it falls in the seasonal gaps of the line light curve. The lower 2×2 panels of Fig. 5 show an example of the lag distributions from the simulated light curves, and the recovered lags are consistent with the input lag. The same figures for other reference AGN and input lags are available in the supplementary material. There are

three realizations for $\tau_i = 370.1$ d and six realizations for $\tau_i = 540.8$ d that pass the final sample criteria. None of them are 'false positives' as defined in Section 4.1. While this simulation still does not perfectly mimic the behaviour of the Mg II line due to the difference between H β and Mg II and the simplifications used in the method, it is a qualitative verification of our lag selection criteria based on real AGN light curves rather than idealized models.

4.3 Comparison of lag selection criteria

In addition to the final sample, there are AGNs that only pass the criteria for Method 1 or 2. Fig. 6 shows examples of the lag distributions for these AGNs. DES J024611.20+003134.30 passes the Method 1 criteria with a high major peak fraction f_{peak} of the JAVELIN lag distribution, while it is excluded by the Method 2 criteria due to the large mean absolute deviation caused by the aliasing peaks. DES J004111.46−441014.41 marginally passes the Method 2 criteria with a mean absolute deviation close to the threshold, while it is excluded by the Method 1 criteria due to significant aliasing when allowing negative lags. The lag distributions of both examples are ambiguous and dominated by aliasing signals at the seasonal gaps. This qualitatively shows how combining the two criteria can help exclude ambiguous measurements. The symmetric lag prior range in Method 1 reduces the strength of spurious signals caused by only allowing positive lags, while Method 2 is more sensitive to spurious lag distributions with multiple aliasing peaks at significantly different lags.

To quantitatively compare the reliability of different samples, we repeat the FPR calculation in Section 4.1 but use only one set of criteria to select successful lag measurements. Fig. 4 compares the FPR from a single set of criteria to that from the final sample criteria. Using just one set of criteria results in a larger overall FPR than using both. We then analyse the simulated light curves from Section 4.2 using only one set of selection criteria. For an input lag $\tau_i = 370.1$ d, we get three incorrect lag recoveries when only using the Method 1 criteria. For $\tau_i = 540.8$ d, we get one incorrect lag recovery when only using the Method 2 criteria. This indicates that only using one set of criteria is less robust than the combined criteria.

Another commonly used method of assessing the sample reliability is comparing the number of positive and negative lag measurements (e.g. Grier et al. 2019; Homayouni et al. 2020; Y21). The negative lags are from artefacts, so the comparison between the number of positive and negative lags gives an overall estimate of the contamination from spurious detection. For Method 1, we get 14 negative lags and 48 positive lags. The comparison is not directly applicable to Method 2 since it only allows positive lags when running JAVELIN and ICCF. We do a one-sided search of $[-1000, 0]$ d as symmetric to the positive prior $[0, 1000]$ d while keeping other criteria of Method 2 the same. This gives 29 negative lags compared to 56 positive lags. When combing the two sets of criteria, we get the 25 positive lags in the final sample and no negative lags. These comparisons indicate that the final sample is less contaminated by artefacts than the samples obtained using only a single set of criteria. There are likely to be physical lag measurements in the single-method samples. However, since they are more likely to be contaminated by spurious lags than our final sample and could increase the risk of biasing the R–L relation, we do not include them in our R–L relation. The light curves of the single-method sample are available in the supplementary material.

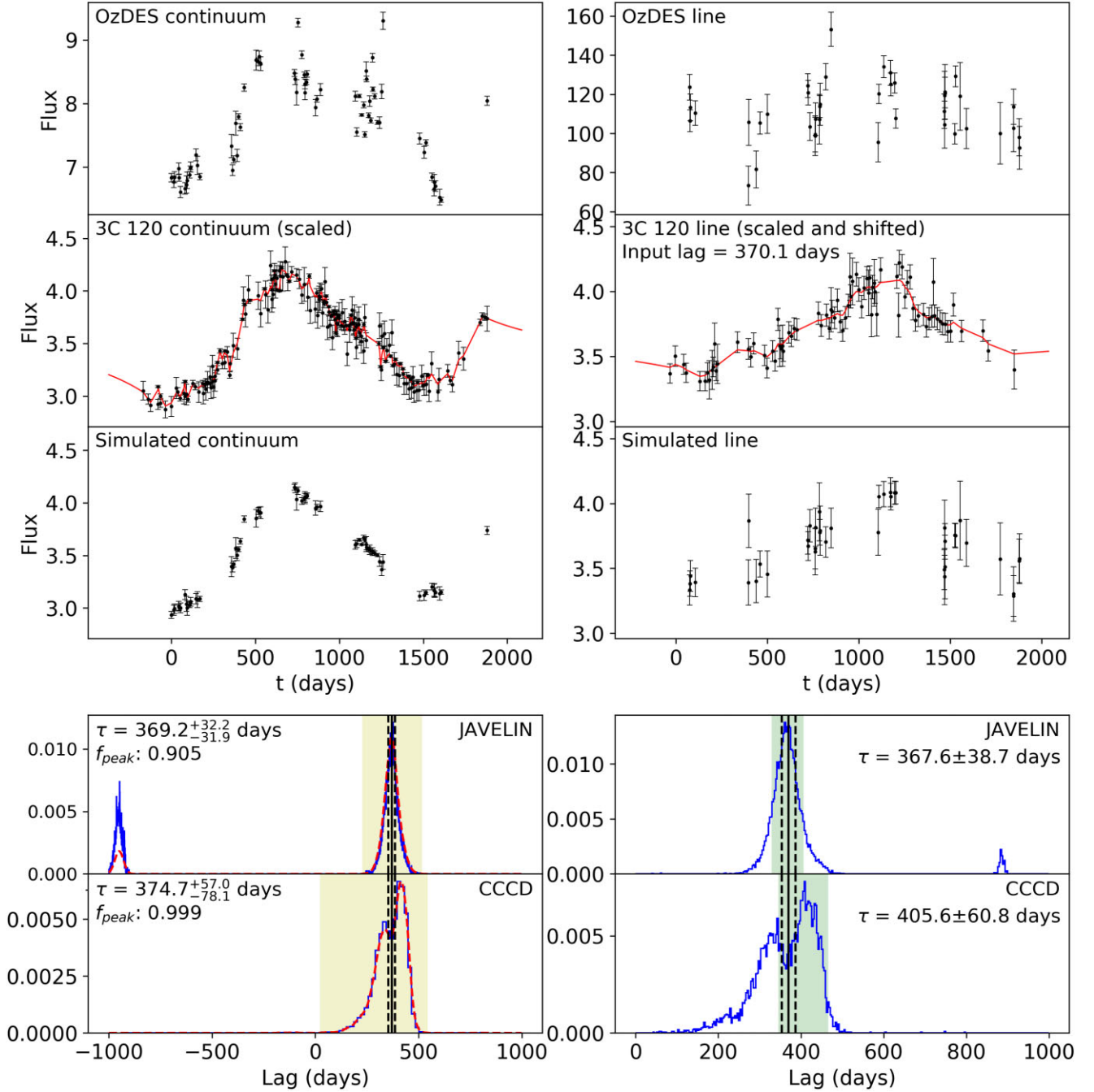**Figure 5.** Examples of the simulations based on the observed light curves of local AGN. (*Upper 3 × 2 panels*) Procedure for creating simulated light curves based on the reference light curves. The light curves are in arbitrary units and the absolute flux scales have no effect on our simulations. The left and right columns show the continuum and line light curves, respectively. The top row shows the OzDES continuum and line light curves of DES J003207.44−433049.00. The middle row shows the scaled reference light curves based on 3C 120. The input lag between the scaled reference light curves is 370.1 d, which equals the observed lag between the OzDES light curves of DES J003207.44−433049.00. The red lines represent the best-fitting light curves from JAVELIN. The bottom row shows the simulated light curves, which have the same cadence and variability amplitude as the OzDES light curves in the top row. (*Lower 2 × 2 panels*) Lag distributions from the simulated light curves. The left and right columns show results from the symmetric and positive lag priors, respectively. The black solid line is drawn at the input lag. The black dashed lines show the 1σ uncertainty of the input lag, which is the uncertainty of the lag between the original reference light curves multiplied by the baseline scaling factor X_t. Other symbols have the same meanings as in Fig. 3.

Table 3. The AGN used for the simulations in Section 4.2. Column (1) gives the object name. These objects generally have light curves for multiple continuum bands and emission lines. Columns (2) and (3) give the continuum band and emission line we adopt for the reference light curves. Column (4) gives the source of the reference light curves. NGC 5548 has light curves from different seasons, which we use as separate reference light curves.

Name	Continuum band	Line	Source
NGC 5548	1367 Å	Ly α	De Rosa et al. (2015)
Mrk 335	*V* band	H β	Grier et al. (2012)
Mrk 1501	*V* band	H β	Grier et al. (2012)
3C 120	*V* band	H β	Grier et al. (2012)
Mrk 6	*V* band	H β	Grier et al. (2012)
PG 2130+099	*V* band	H β	Grier et al. (2012)
Mrk 704	5100 Å	H β	De Rosa et al. (2018)
NGC 3227	5100 Å	H β	De Rosa et al. (2018)
NGC 3516	5100 Å	H β	De Rosa et al. (2018)
NGC 4151	5100 Å	H β	De Rosa et al. (2018)
NGC 5548	5100 Å	H β	De Rosa et al. (2018)
Mrk 142	5100 Å	H β	Du et al. (2014)
Mrk 382	*V* band	H β	Wang et al. (2014)

5 BLACK HOLE MASS AND *R–L* RELATION

We calculate the black hole mass with equation (1), and parametrize the line width using the line dispersion defined by

$$\sigma_{\text{line}}^2 = \left[\int \lambda^2 P(\lambda) d\lambda \Big/ \int P(\lambda) d\lambda \right] - P_0(\lambda)^2, \qquad (13)$$

where $P(\lambda)$ is the line profile and $P_0(\lambda)$ is the first moment of $P(\lambda)$. Using the line dispersion as the line width estimator generally provides better black hole mass estimates than using the full width at half-maximum (e.g. Peterson et al. 2004; Dalla Bontà et al. 2020). Given the low SNR of our single-epoch spectra, we measure the line dispersion from the mean spectra instead of the rms spectra commonly used in RM studies. Previous studies show that the mean spectra line dispersion reasonably approximates the rms spectra line

dispersion (e.g. Dalla Bontà et al. 2020; Wang et al. 2020). We adopt a virial factor of $f = 4.31 \pm 1.05$ from Grier et al. (2013b). Table 1 gives the line dispersion and black hole mass estimates for our final sample. The black hole masses have an uncertainty of $\sim$0.4 dex, which is mainly from the intrinsic scatter in the calibration of the virial factor (e.g. Peterson 2014). We do not include detailed estimates of other measurement uncertainties since they are small relative to the uncertainty in the virial factor.

Fig. 7 shows the Mg II *R–L* relation for our final sample. Before this work, the largest Mg II lag sample was the 24 sources in the gold sample of Homayouni et al. (2020). Our sample nearly doubles the total number of high-quality Mg II lags. We significantly extend the Mg II lag measurements towards higher redshifts and bridge the gap in luminosity between the Homayouni et al. (2020) sample and the high luminosity sources studied by Lira et al. (2018), Czerny et al. (2019), and Zajaček et al. (2020, 2021), as illustrated in Figs 1 and 7. Compared to the OzDES Y5 results from Y21, the full OzDES Mg II lag sample covers about a factor of 5 wider range in $\log(\lambda L_{3000})$, which allows us to better constrain the *R–L* relation.

We parametrize the *R–L* relation as

$$\log(R/\text{lt-days}) = \alpha \log[L/(10^{45} \text{ erg s}^{-1})] + \beta, \qquad (14)$$

with an intrinsic scatter σ_{rl}. We fit our final sample with the MCMC sampler EMCEE (Foreman-Mackey et al. 2013) and get best-fitting parameters $\alpha = 0.39 \pm 0.08$, $\beta = 2.07 \pm 0.04$, and $\sigma_{\text{rl}} = 0.15^{+0.03}_{-0.02}$. Fig. 7 shows the best-fitting *R–L* relation and uncertainties. The slope is shallower than the $\sim$0.5 slope of the H β *R–L* relations (e.g. Bentz et al. 2013), although they are marginally consistent at 1.5σ. The slope is broadly consistent with the Homayouni et al. (2020) gold sample given their uncertainties, but our intrinsic scatter is significantly smaller than the $\sim$0.36-dex intrinsic scatter in their sample. It is marginally larger than the intrinsic scatter $\sigma_{\text{rl}} \sim$0.13 dex of the H β *R–L* relation from Bentz et al. (2013) but within uncertainties, while it is smaller than $\sigma_{\text{rl}} \sim 0.19$ dex of the H β *R–L* relation from Du et al. (2016) after they accounted for the effect of Eddington ratio. This indicates that the Mg II line may still have
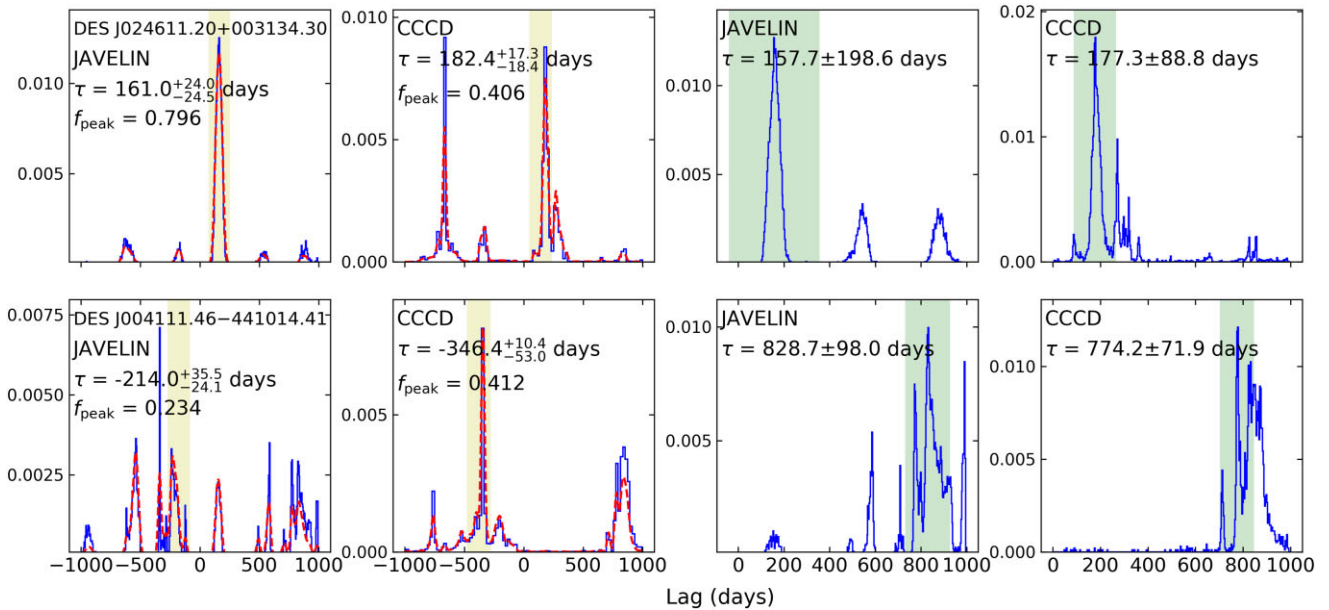

Figure 6. Lag distributions of DES J024611.20+003134.30 (upper row) that only passes the Method 1 criteria and DES J004111.46−441014.41 (lower row) that only passes the Method 2 criteria. The two leftmost columns show the JAVELIN and ICCF lag distributions with a symmetric prior, while the two rightmost columns show results with a positive prior. Other symbols have the same meanings as in Fig. 3.
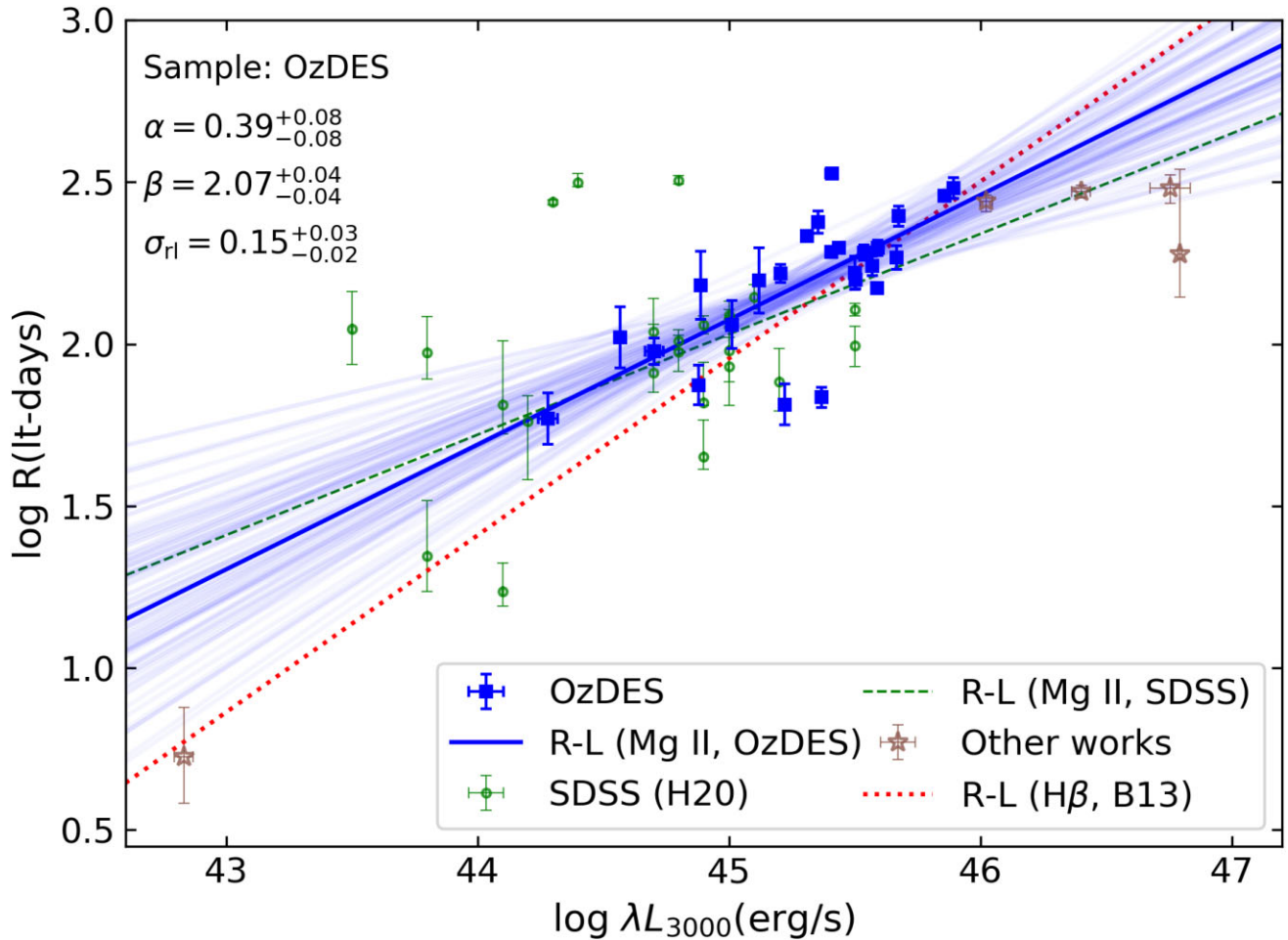
Figure 7. Mg II *R–L* relation from the OzDES RM project and previous works. The blue squares are our high-quality measurements from the full 6 yr of data. The green circles are the gold sample of Homayouni et al. (2020). The brown stars are measurements from Metzroth et al. (2006), Lira et al. (2018), Zajaček et al. (2020, 2021), and Prince et al. (2022). The blue solid line shows the best-fitting Mg II *R–L* relation constrained using our final sample with the slope α and intrinsic scatter $\sigma_{\rm rl}$ shown in the upper left corner. The lighter blue lines are 100 realizations randomly drawn from the MCMC chain, which illustrates the uncertainty of our *R–L* relation. The green dashed line shows the Mg II *R–L* relation from Homayouni et al. (2020). The red dotted line shows the H β *R–L* relation from Bentz et al. (2013) with a slope of ∼0.5 and an intrinsic scatter of ∼0.13 dex. We use the bolometric correction from Richards et al. (2006) to convert the 3000-Å monochromatic luminosity to 5100 Å for the H β *R–L* relation.

a tight *R–L* relation despite its weaker response to the continuum variability (e.g. Guo et al. 2020).

For completeness, we also fit the *R–L* relation including all Mg II lags from the literature. The best-fitting parameters are $\alpha = 0.3 \pm 0.05$, $\beta = 2.07 \pm 0.03$, and $\sigma_{\rm rl} = 0.24^{+0.03}_{-0.02}$. This gives a shallower slope and larger intrinsic scatter, although the intrinsic scatter is still smaller than that from Homayouni et al. (2020) and is close to the ∼0.26-dex intrinsic scatter from Du et al. (2016) without considering the Eddington ratio. The lags from different works are selected using different criteria and have different definitions of uncertainties, which could bias the *R–L* relation, so we adopt our fit to only the OzDES sample as the most robust Mg II *R–L* relation.

5.1 Effect of iron line strength

Previous studies measured smaller H β lags from AGN with higher Eddington ratios at fixed luminosities (e.g. Du et al. 2016, 2018; Dalla Bontà et al. 2020). If also true of Mg II, it could explain the shallower slope of our Mg II *R–L* relation. However, the Eddington ratios in previous studies depend on the virial black hole mass estimates

and therefore depend on the lag measurements themselves. One independent indicator of the Eddington ratio is the strength of the iron emission (e.g. Boroson 2002; Negrete et al. 2018; Panda, Marziani & Czerny 2019). Du & Wang (2019) reduced the intrinsic scatter of the *R–L* relation by adding the ratio $\mathcal{R}_{\rm Fe,optical}$ of the optical iron line flux to the H β line flux as a third parameter, while Khadka et al. (2022b) found no significant reduction of the intrinsic scatter after including $\mathcal{R}_{\rm Fe,optical}$. This discrepancy could be because Khadka et al. (2022b) constrained the *R–L* relation and the cosmological parameters at the same time, while Du & Wang (2019) fixed the cosmological parameters. Khadka et al. (2022a) performed similar analysis with the ratio $\mathcal{R}_{\rm Fe}$ of the ultraviolet iron flux to the Mg II flux and found that it had little impact on the Mg II *R–L* relation. In this section, we probe the effect of $\mathcal{R}_{\rm Fe}$ on our Mg II *R–L* relation.

For each spectroscopic epoch, we calculate the iron ratio as $\mathcal{R}_{\rm Fe} = F_{\rm Fe}/F_{\rm line}$, where $F_{\rm Fe}$ is the integrated iron flux over rest frame 2250–2650 Å and $F_{\rm line}$ is the Mg II line flux. We derive the mean $\langle \mathcal{R}_{\rm Fe} \rangle$ and the standard deviation $S_{\mathcal{R}_{\rm Fe}}$ over $N_{\rm e}$ epochs. The uncertainty of the mean is $\sigma_{\mathcal{R}_{\rm Fe}} = S_{\mathcal{R}_{\rm Fe}}/\sqrt{N_{\rm e}}$. Table 1 gives the iron ratio $\langle \mathcal{R}_{\rm Fe} \rangle$ and its uncertainty $\sigma_{\mathcal{R}_{\rm Fe}}$ for the AGN in our final sample. Fig. 8 shows
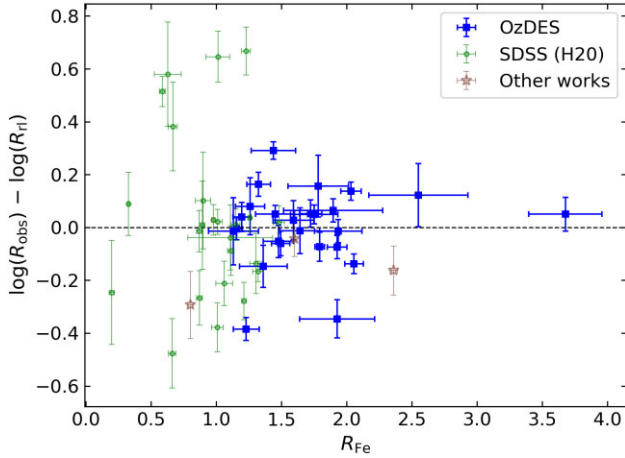
Figure 8. Deviation of the observed lag R_{obs} from the prediction R_{rl} of the Mg II R–L relation based on the OzDES sample versus the iron ratio $\mathcal{R}_{Fe}$. The black dashed line is drawn where the observed lag falls exactly on the R–L relation. The coloured symbols have same meanings as in Fig. 7.

the deviation of the observed lags from our Mg II R–L relation versus the iron ratio $\mathcal{R}_{Fe}$. It also includes the AGN from previous Mg II RM studies, with the exception of Metzroth et al. (2006) and Lira et al. (2018) who did not report $\mathcal{R}_{Fe}$ measurements. There is no significant correlation between the deviation from the R–L relation and the iron ratio $\mathcal{R}_{Fe}$.

To quantify the potential improvement from the two-parameter R–L relation to a three-parameter relation with $\mathcal{R}_{Fe}$, we consider the two parametrizations studied in Khadka et al. (2022a):

$$\log(R/\text{lt-days}) = \alpha \log[L/(10^{45}\,\text{erg s}^{-1})] + \beta + \gamma \mathcal{R}_{Fe} \quad (15)$$

and

$$\log(R/\text{lt-days}) = \alpha \log[L/(10^{45}\,\text{erg s}^{-1})] + \beta + \gamma \log(\mathcal{R}_{Fe}). \quad (16)$$

For the OzDES sample, we obtain an intrinsic scatter of $\sigma_{rl} = 0.15^{+0.03}_{-0.02}$ for both parametrizations. When including the literature lags, both parametrizations give $\sigma_{rl} = 0.22^{+0.03}_{-0.02}$. The intrinsic scatters of these three-parameter correlations are close to the two-parameter R–L relation. These results indicate that the iron ratio $\mathcal{R}_{Fe}$ has little impact on the Mg II R–L relation, in agreement with the results of Khadka et al. (2022a).

6 SUMMARY

We use 6 yr of photometry and spectroscopy from the OzDES RM project to measure Mg II lags. We calibrate the spectra using the pipeline developed by Hoormann et al. (2019) based on the DES photometry and estimate the calibration uncertainties using the Monte Carlo approach from Y21 based on the F stars observed in the OzDES fields. We use the algorithm from Y21 to model and subtract the continuum + iron emission around the Mg II line. We define quantitative criteria to select reliable measurements and verify the lag reliability using simulations based on both the DRW stochastic process and the observed light curves of AGN. Our major results are as follows:

(i) We obtain high-quality Mg II lag measurements for 25 quasars. Seven quasars were presented in Y21, and their lags from the full 6-yr light curves are consistent with those from Y21 based on the first 5 yr of data. Our sample substantially increases the number of Mg II lags and extends the R–L relation to higher redshifts and luminosities.

(ii) Our sample provides a new constraint of the Mg II R–L relation with a slope $\alpha = 0.39 \pm 0.08$, an intercept $\beta = 2.07 \pm 0.04$, and an intrinsic scatter $\sigma_{rl} = 0.15^{+0.03}_{-0.02}$. The slope is consistent with the Mg II R–L relation from Homayouni et al. (2020), while it is shallower than the H β R–L relation based on local AGN. The intrinsic scatter is significantly smaller than that from Homayouni et al. (2020) and is close to that of the H β R–L relations, which makes it promising to apply our R–L relation to large samples of single-epoch mass estimates and SMBH demographic studies at cosmic noon.

(iii) The residual from the R–L relation has no significant correlation with the relative iron strength $\mathcal{R}_{Fe}$ as an indicator of the Eddington ratio. Adding $\mathcal{R}_{Fe}$ as a third parameter does not reduce the intrinsic scatter of the R–L relation.

Future RM campaigns based on wide-field photometric and spectroscopic surveys, such as the Rubin Observatory Legacy Survey of Space and Time (LSST; e.g. LSST Science Collaboration 2009), the Black Hole Mapper in SDSS-V (e.g. Kollmeier et al. 2017), and the Time-Domain Extragalactic Survey with the 4-metre Multi-Object Spectroscopic Telescope (4MOST, e.g. Swann et al. 2019), should provide larger sample of lag measurements and better constraints of the R–L relation. In addition to deeper observations with future facilities, the optimization of survey strategy is critical for successful RM campaigns. For example, Malik et al. (2022) used simulated light curves to study the effect of observational windows on the lag recovery in future surveys. They found that maximizing the length of the observing seasons is important especially for reducing the aliasing effects that significantly affect the lag measurements, although observing polar fields could be challenging due to the higher airmass. The spectroscopic calibration is also critical for future RM studies, since the calibration uncertainty could contribute a significant fraction of the error budget for deep observations. There are three AGNs in our final sample where the calibration uncertainty dominates the error budget. Calibration uncertainties will become increasingly important for deeper future surveys.

The Collaborating Institutions are Argonne National Laboratory, the University of California at Santa Cruz, the University of Cambridge, Centro de Investigaciones Energéticas, Medioambientales y Tecnológicas-Madrid, the University of Chicago, University College London, the DES-Brazil Consortium, the University of Edinburgh, the Eidgenössische Technische Hochschule (ETH) Zürich, Fermi National Accelerator Laboratory, the University of Illinois at Urbana-Champaign, the Institut de Ciències de l'Espai (IEEC/CSIC), the Institut de Física d'Altes Energies, Lawrence Berkeley National Laboratory, the Ludwig-Maximilians Universität München and the associated Excellence Cluster Universe, the University of Michigan, NSF's NOIRLab, the University of Nottingham, the Ohio State University, the University of Pennsylvania, the University of Portsmouth, SLAC National Accelerator Laboratory, Stanford University, the University of Sussex, Texas A&M University, and the OzDES Membership Consortium.

DATA AVAILABILITY

We present supplementary materials in the online journal:

(i) Figures of the single-epoch spectra in the same format as Fig. 2 for the final sample sources. These figures also include the co-added and rms spectra for each source.

(ii) Machine-readable light curves for the final sample sources and sources that only pass one set of criteria.

(iii) Figures of the light curves and lag measurements in the same format as Fig. 3 for the final sample sources.

(iv) Figures of the simulated light curves based on the observed light curves of local AGN (Section 4.2). They are in the same format as Fig. 5, but for other reference AGN and input lag.

The underlying DES and OzDES data are available in Abbott et al. (2021) and Lidman et al. (2020).

REFERENCES

Abbott T. M. C. et al., 2018, ApJS, 239, 18
Abbott T. M. C. et al., 2021, ApJS, 255, 20
Barth A. J. et al., 2011a, ApJ, 732, 121
Barth A. J. et al., 2011b, ApJ, 743, L4
Barth A. J. et al., 2013, ApJ, 769, 128
Barth A. J., Boizelle B. D., Darling J., Baker A. J., Buote D. A., Ho L. C., Walsh J. L., 2016, ApJ, 822, L28
Bentz M. C., Peterson B. M., Netzer H., Pogge R. W., Vestergaard M., 2009, ApJ, 697, 160
Bentz M. C. et al., 2013, ApJ, 767, 149
Bentz M. C. et al., 2014, ApJ, 796, 8
Bentz M. C., Cackett E. M., Crenshaw D. M., Horne K., Street R., Ou-Yang B., 2016, ApJ, 830, 136
Blandford R. D., McKee C. F., 1982, ApJ, 255, 419
Boroson T. A., 2002, ApJ, 565, 78
Childress M. J. et al., 2017, MNRAS, 472, 273
Czerny B. et al., 2019, ApJ, 880, 46
Dalla Bontà E. et al., 2020, ApJ, 903, 112
Denney K. D. et al., 2010, ApJ, 721, 715
De Rosa G. et al., 2015, ApJ, 806, 128
De Rosa G. et al., 2018, ApJ, 866, 133
Du P., Wang J.-M., 2019, ApJ, 886, 42
Du P. et al., 2014, ApJ, 782, 45
Du P. et al., 2015, ApJ, 806, 22
Du P. et al., 2016, ApJ, 825, 126
Du P. et al., 2018, ApJ, 856, 6
Fausnaugh M. M. et al., 2017, ApJ, 840, 97
Flaugher B. et al., 2015, AJ, 150, 150
Foreman-Mackey D., Hogg D. W., Lang D., Goodman J., 2013, PASP, 125, 306
Gaskell C. M., Peterson B. M., 1987, ApJS, 65, 1
Gebhardt K., Thomas J., 2009, ApJ, 700, 1690
Goad M. R. et al., 2016, ApJ, 824, 11
Gray P. M., Taylor K., Parry I. R., Lewis I. J., Sharples R. M., 1993, in Gray P. M., ed., ASP Conf. Ser. Vol. 37, Fiber Optics in Astronomy II. Astron. Soc. Pac., San Francisco, p. 145
Grier C. J. et al., 2012, ApJ, 755, 60
Grier C. J. et al., 2013a, ApJ, 764, 47
Grier C. J. et al., 2013b, ApJ, 773, 90
Grier C. J. et al., 2017, ApJ, 851, 21
Grier C. J. et al., 2019, ApJ, 887, 38
Guo H. et al., 2020, ApJ, 888, 58
Homayouni Y. et al., 2020, ApJ, 901, 55
Hoormann J. K. et al., 2019, MNRAS, 487, 3650
Horne K. et al., 2021, ApJ, 907, 76
Hu C. et al., 2021, ApJS, 253, 20
Jones E. et al., 2001, SciPy: Open Source Scientific Tools for Python, available at http://www.scipy.org/
Kasliwal V. P., Vogeley M. S., Richards G. T., Williams J., Carini M. T., 2015, MNRAS, 453, 2075
Kaspi S., Smith P. S., Netzer H., Maoz D., Jannuzi B. T., Giveon U., 2000, ApJ, 533, 631
Kaspi S., Brandt W. N., Maoz D., Netzer H., Schneider D. P., Shemmer O., 2007, ApJ, 659, 997
Kelly B. C., Shen Y., 2013, ApJ, 764, 45
Khadka N., Zajaček M., Panda S., Martínez-Aldama M. L., Ratra B., 2022a, MNRAS, 515, 3729
Khadka N., Martínez-Aldama M. L., Zajaček M., Czerny B., Ratra B., 2022b, MNRAS, 513, 1985
King A. L. et al., 2015, MNRAS, 453, 1701
Kollmeier J. A. et al., 2017, preprint (arXiv:1711.03234)
Korista K. T., Goad M. R., 2004, ApJ, 606, 749
Kormendy J., Richstone D., 1995, ARA&A, 33, 581
Lawther D., Goad M. R., Korista K. T., Ulrich O., Vestergaard M., 2018, MNRAS, 481, 533
Li Y.-R. et al., 2018, ApJ, 869, 137
Li J. et al., 2019, ApJ, 884, 119
Li S.-S. et al., 2021, ApJ, 920, 9
Lidman C. et al., 2020, MNRAS, 496, 19
Lira P. et al., 2018, ApJ, 865, 56
LSST Science Collaboration, 2009, preprint (arXiv:0912.0201)
Lu K.-X. et al., 2016, ApJ, 827, 118

Malik U. et al., 2022, MNRAS, 516, 323

Martínez-Aldama M. L., Zajaček M., Czerny B., Panda S., 2020, ApJ, 903, 86

Metzroth K. G., Onken C. A., Peterson B. M., 2006, ApJ, 647, 901

Mudd D. et al., 2018, ApJ, 862, 123

Mushotzky R. F., Edelson R., Baumgartner W., Gandhi P., 2011, ApJ, 743, L12

Negrete C. A. et al., 2018, A&A, 620, A118

Panda S., Marziani P., Czerny B., 2019, ApJ, 882, 79

Pei L. et al., 2014, ApJ, 795, 38

Penton A. et al., 2022, MNRAS, 509, 4008

Peterson B. M., 1993, PASP, 105, 247

Peterson B. M., 2014, Space Sci. Rev., 183, 253

Peterson B. M., Wanders I., Horne K., Collier S., Alexander T., Kaspi S., Maoz D., 1998, PASP, 110, 660

Peterson B. M. et al., 2004, ApJ, 613, 682

Peterson B. M. et al., 2005, ApJ, 632, 799

Prince R. et al., 2022, A&A, 667, A42

Richards G. T. et al., 2006, ApJS, 166, 470

Rodríguez-Pascual P. M. et al., 1997, ApJS, 110, 9

Salviander S., Shields G. A., Gebhardt K., Bonning E. W., 2007, ApJ, 662, 131

Shen Y. et al., 2015, ApJS, 216, 4

Shen Y. et al., 2016, ApJ, 818, 30

Smith G. A. et al., 2004, in Moorwood A. F. M., Masanori I., eds, Proc. SPIE Conf. Ser. Vol. 5492, Ground-based Instrumentation for Astronomy. SPIE, Bellingham, p. 410

Smith K. L., Mushotzky R. F., Boyd P. T., Malkan M., Howell S. B., Gelino D. M., 2018, ApJ, 857, 141

Stone Z. et al., 2022, MNRAS, 514, 164

Sun M., Grier C. J., Peterson B. M., 2018, Astrophysics Source Code Library, record ascl:1805.032

Swann E. et al., 2019, Messenger, 175, 58

Trevese D., Perna M., Vagnetti F., Saturni F. G., Dadina M., 2014, ApJ, 795, 164

Tsuzuki Y., Kawara K., Yoshii Y., Oyabu S., Tanabé T., Matsuoka Y., 2006, ApJ, 650, 57

Ueda Y., Akiyama M., Hasinger G., Miyaji T., Watson M. G., 2014, ApJ, 786, 104

Vaughan S., Edelson R., Warwick R. S., Uttley P., 2003, MNRAS, 345, 1271

Verner E. M., Verner D. A., Korista K. T., Ferguson J. W., Hamann F., Ferland G. J., 1999, ApJS, 120, 101

Vestergaard M., Osmer P. S., 2009, ApJ, 699, 800

Vestergaard M., Wilkes B. J., 2001, ApJS, 134, 1

Vestergaard M., Fan X., Tremonti C. A., Osmer P. S., Richards G. T., 2008, ApJ, 674, L1

Vivian U. et al., 2022, ApJ, 925, 52

Wang J.-M. et al., 2014, ApJ, 793, 108

Wang S. et al., 2020, ApJ, 903, 51

Williams P. R. et al., 2021, ApJ, 911, 64

Wills B. J., Netzer H., Uomoto A. K., Wills D., 1980, ApJ, 237, 319

Wills B. J., Netzer H., Wills D., 1985, ApJ, 288, 94

Wolf C., Wisotzki L., Borch A., Dye S., Kleinheinrich M., Meisenheimer K., 2003, A&A, 408, 499

Yu Z. et al., 2020a, ApJS, 246, 16

Yu Z., Kochanek C. S., Peterson B. M., Zu Y., Brandt W. N., Cackett E. M., Fausnaugh M. M., McHardy I. M., 2020b, MNRAS, 491, 6045

Yu Z. et al., 2021, MNRAS, 507, 3771 (Y21)

Yuan F. et al., 2015, MNRAS, 452, 3047

Zajaček M. et al., 2020, ApJ, 896, 146

Zajaček M. et al., 2021, ApJ, 912, 10

Zhang Z.-X. et al., 2019, ApJ, 876, 49

Zu Y., Kochanek C. S., Peterson B. M., 2011, ApJ, 735, 80

Zu Y., Kochanek C. S., Kozłowski S., Udalski A., 2013, ApJ, 765, 106

[1]*Department of Astronomy, The Ohio State University, Columbus, OH 43210, USA*

[2]*Center of Cosmology and Astro-Particle Physics, The Ohio State University, Columbus, OH 43210, USA*

[3]*Radcliffe Institute for Advanced Study, Harvard University, Cambridge, MA 02138, USA*

[4]*School of Mathematics and Physics, University of Queensland, Brisbane, QLD 4072, Australia*

[5]*ARC Centre of Excellence for All-sky Astrophysics (CAASTRO), 44 Rosehill Street, Redfern, NSW 2016, Australia*

[6]*Sydney Institute for Astronomy, School of Physics, The University of Sydney, A28, Sydney, NSW 2006, Australia*

[7]*Australian Astronomical Observatory, North Ryde, NSW 2113, Australia*

[8]*Research School of Astronomy and Astrophysics, Australian National University, Canberra, ACT 2611, Australia*

[9]*Laboratório Interinstitucional de e-Astronomia-LIneA, Rua Gal. José Cristino 77, Rio de Janeiro, RJ-20921-400, Brazil*

[10]*Fermi National Accelerator Laboratory, P. O. Box 500, Batavia, IL 60510, USA*

[11]*Institut d'Astrophysique de Paris, Sorbonne Universités, UPMC Univ Paris 06, UMR 7095, F-75014 Paris, France*

[12]*Institut d'Astrophysique de Paris, CNRS, UMR 7095, F-75014 Paris, France*

[13]*University Observatory, Faculty of Physics, Ludwig-Maximilians-Universität, Scheinerstraße 1, D-81679 Munich, Germany*

[14]*Department of Physics & Astronomy, University College London, Gower Street, London WC1E 6BT, UK*

[15]*Instituto de Astrofisica de Canarias, E-38205 La Laguna, Tenerife, Spain*

[16]*Departamento de Astrofísica, Universidad de La Laguna, E-38206 La Laguna, Tenerife, Spain*

[17]*INAF-Osservatorio Astronomico di Trieste, via G. B. Tiepolo 11, I-34143 Trieste, Italy*

[18]*Department of Astronomy, University of Illinois at Urbana-Champaign, 1002 W. Green Street, Urbana, IL 61801, USA*

[19]*Center for Astrophysical Surveys, National Center for Supercomputing Applications, 1205 West Clark Street, Urbana, IL 61801, USA*

[20]*Institut de Física d'Altes Energies (IFAE), The Barcelona Institute of Science and Technology, Campus UAB, E-08193 Bellaterra (Barcelona), Spain*

[21]*Institute for Fundamental Physics of the Universe, via Beirut 2, I-34014 Trieste, Italy*

[22]*Astronomy Unit, Department of Physics, University of Trieste, via Tiepolo 11, I-34131 Trieste, Italy*

[23]*Hamburger Sternwarte, Universität Hamburg, Gojenbergsweg 112, D-21029 Hamburg, Germany*

[24]*Centro de Investigaciones Energéticas, Medioambientales y Tecnológicas (CIEMAT), Avda. Complutense 40, E-28040 Madrid, Spain*

[25]*Jet Propulsion Laboratory, California Institute of Technology, 4800 Oak Grove Dr, Pasadena, CA 91109, USA*

[26]*Institute of Theoretical Astrophysics, University of Oslo, P. O. Box 1029, Blindern, NO-0315 Oslo, Norway*

[27]*Instituto de Fisica Teorica UAM/CSIC, Universidad Autonoma de Madrid, E-28049 Madrid, Spain*

[28]*Department of Physics and Astronomy, University of Pennsylvania, Philadelphia, PA 19104, USA*

[29]*Department of Astronomy, University of Michigan, Ann Arbor, MI 48109, USA*

[30]*Department of Physics, University of Michigan, Ann Arbor, MI 48109, USA*

[31]*Observatório Nacional, Rua Gal. José Cristino 77, Rio de Janeiro, RJ-20921-400, Brazil*

[32]*Santa Cruz Institute for Particle Physics, Santa Cruz, CA 95064, USA*

[33]*Department of Physics, The Ohio State University, Columbus, OH 43210, USA*

[34]*Center for Astrophysics | Harvard & Smithsonian, 60 Garden Street, Cambridge, MA 02138, USA*

[35]*Lowell Observatory, 1400 Mars Hill Road, Flagstaff, AZ 86001, USA*

[36]*Institució Catalana de Recerca i Estudis Avançats, E-08010 Barcelona, Spain*

[37]*Department of Physics, University of Surrey, Guildford, Surrey, GU2 7XH, UK*

38*Institute of Astronomy, University of Cambridge, Madingley Road, Cambridge CB3 0HA, UK*

39*Department of Astrophysical Sciences, Princeton University, Peyton Hall, Princeton, NJ 08544, USA*

40*Department of Physics and Astronomy, University of Sussex, Pevensey Building, Brighton BN1 9QH, UK*

41*School of Physics and Astronomy, University of Southampton, Southampton SO17 1BJ, UK*

42*Computer Science and Mathematics Division, Oak Ridge National Laboratory, Oak Ridge, TN 37831, USA*

43*Institute of Cosmology and Gravitation, University of Portsmouth, Portsmouth PO1 3FX, UK*

44*Cerro Tololo Inter-American Observatory, NSF's National Optical-Infrared Astronomy Research Laboratory, Casilla 603, La Serena, 1700000, Chile*

45*Lawrence Berkeley National Laboratory, 1 Cyclotron Road, Berkeley, CA 94720, USA*

This paper has been typeset from a TEX/LATEX file prepared by the author.